ARTICLE

Check for updates

Resurgence of superconductivity and the role of dxy hole band in FeSe$_{1-x}$Te$_x$

Archie B. Morfoot [1,2✉], Timur K. Kim [2], Matthew D. Watson [2], Amir A. Haghighirad [1,3], Shiv J. Singh [1], Nick Bultinck[4] & Amalia I. Coldea [1✉]

Iron-chalcogenide superconductors display rich phenomena caused by orbital-dependent band shifts and electronic correlations. Additionally, they are potential candidates for topological superconductivity due to the band inversion between the Fe d bands and the chalcogen p_z band. Here we present a detailed study of the electronic structure of the nematic superconductors FeSe$_{1-x}$Te$_x$ ($0 < x < 0.4$) using angle-resolved photoemission spectroscopy to understand the role of orbital-dependent band shifts, electronic correlations and the chalcogen band. We assess the changes in the effective masses using a three-band low energy model, and the band renormalization via comparison with DFT band structure calculations. The effective masses decrease for all three-hole bands inside the nematic phase, followed by a strong increase for the band with d_{xy} orbital character. Interestingly, this nearly-flat d_{xy} band becomes more correlated as it shifts towards the Fermi level with increasing Te concentrations and as the second superconducting dome emerges. Our findings suggests that the d_{xy} hole band, which is very sensitive to the chalcogen height, could be involved in promoting an additional pairing channel and increasing the density of states to stabilize the second superconducting dome in FeSe$_{1-x}$Te$_x$. This simultaneous shift of the d_{xy} hole band and enhanced superconductivity is in contrast with FeSe$_{1-x}$S$_x$.

[1] Clarendon Laboratory, Department of Physics, University of Oxford, Parks Road, Oxford OX1 3PU, UK. [2] Diamond Light Source, Harwell Science and Innovation Campus, Didcot OX11 0DE, UK. [3] Institute for Quantum Materials and Technologies, Karlsruhe Institute of Technology, 76131 Karlsruhe, Germany. [4] Rudolf Peierls Centre for Theoretical Physics, University of Oxford, Parks Road, Oxford OX1 3PU, UK. ✉email: archie.morfoot@physics.ox.ac.uk; amalia.coldea@physics.ox.ac.uk

I ron-chalcogenide superconductors display a wide variety of complex electronic phases due to their multi-band nature, small Fermi-energies and large orbital-dependent electronic correlations[1–3]. These stabilise rich phase diagrams that include electronic nematic and spin-density wave phases[4,5], topological surface states[6] and bring the system in the proximity of a BCS-BEC transition[7]. The electronic nematic phase manifests as a spontaneous breaking of the rotational symmetry induced by orbital and momentum dependent band shifts[8,9]. Studies under small amounts of applied strain along the symmetry breaking channel lead to a divergent elastoresistivity close to the transition temperature, revealing its electronic origin[10–13].

Although, nematic critical fluctuations have been suggested to enhance superconductivity[14], the nematic phase is usually accompanied by a spin-density wave, making it difficult to isolate which interaction is driving the superconductivity[15–18]. Moreover, the finite coupling with the lattice can be detrimental on the critical nematic fluctuations and superconductivity[4,19]. FeSe is a unique system which harbours an extended and tunable nematic electronic phase in the absence of long range magnetic order, whilst still stablizing superconductivity at low temperatures[20]. Studies of the superconducting gap have suggested a $s_{\pm}$ sign-changing pairing symmetry which is consistent with a spin-fluctuation mechanism[21–23], but competing Néel and stripe magnetic fluctuations are found in FeSe[22,24]. In the presence of non-magnetic disorder both superconductivity and nematicity is suppressed in $Fe_{1-x}Cu_xSe$ studies[25].

The nematic order of FeSe can be effectively tuned via isoelectronic substitution of Se with S or Te, and the band structure is very sensitive to the chalcogen height above the conducting planes[13,26]. In addition, the Te substitution causes the chalcogen p_z band to shift down towards the hole pockets of the Fe d bands and induce a band inversion at the Fermi level[27], which could stabilise topological surface states[6,15,28,29]. The orbital dependence of the electronic correlations becomes significant for high Te concentration where the band with d_{xy} orbital character experiences a large increase in effective mass relative to other bands with d_{xz}/d_{yz} orbital character[1,30,31].

Single crystals inside the nematic phase of $FeSe_{1-x}Te_x$ series with low Te content have only recently become available, as the chemical vapour transport techniques have overcome the phase separation[32,33]. Recent studies have determined the super-conducting phase diagram which harbours two superconducting regimes, one dome inside the nematic phase followed by a second dome which emerges at the nematic end point, proposed to be driven by critical nematic fluctuations[34].

In this paper, we report a detailed angle-resolved photoemission spectroscopy (ARPES) study of the nematic $FeSe_{1-x}Te_x$ single crystals and determine the evolution of the low-energy features and the role of electronic correlations. Employing a detailed multi-band model, we extract the effective masses of all three hole bands which decrease with increasing Te concentration as both the nematic order and superconducting phases are suppressed. We find that the effective mass of the hole band with d_{xy} character displays a non-monotonic variation reaching a minimum before increasing significantly with the Te substitution. Simultaneously, the d_{xy} hole band shifts towards the Fermi level, which could open a new pairing channel for superconductivity and an enhancement in the density of states, potentially stabilising a second superconducting dome. The k_z dependence of the ARPES spectra enables us to assess the contribution of the chalcogen p_z band, which is instrumental in the formation of topological superconductivity. Lastly, we explore the evolution of the electron pockets with Te concentration and find that size of the pockets increase, whereas the nematic splitting slowly reduces as the nematic phase has an extended compositional range.

Results

The evolution of the hole bands. The band structure of tetragonal FeSe, which is dominated by the bands with Fe 3d orbital character at the Fermi level (E_F), consists of multiple hole pockets in the centre of the Brillouin zone and electron pockets in the corners of it. Figure 1a shows the measured hole band dispersions along the $A-Z-A$ direction for different compositions of $FeSe_{1-x}Te_x$. To highlight weaker spectral features for some of the bands, we have calculated the corresponding curvature[35], as illustrated in Fig. 1b. We clearly observe two dispersive bands with mixed $d_{xz/yz}$ orbital character, labelled as the α band for the outer hole band and the β band for the inner band. A third much flatter band with dominant d_{xy} orbital character, labelled γ, has a weaker spectral weight and is seen ~ 50 meV below the Fermi level in FeSe[13]. As the intensity of ARPES data is proportional to the matrix elements, which are dependent on the properties of both the incident light and the excited electrons, we also use the linear vertical (LV) polarisation to isolate the β hole band, as shown in Fig. 1c[36]. Moreover, matrix elements suppress significantly the intensity associated with bands of d_{xy} orbital character in both polarisations. Therefore, the γ band is mainly visible via hybridisation with the α and β bands and it can be visualised using the curvature analysis in Fig. 1b.

Next, we discuss the band dispersions of the α and β hole bands shown in Fig. 1b. To quantify precisely their position we use both momentum distribution curves (MDCs) (fitted to pairs of symmetric Lorentzian peaks in Fig. 1d) and the maximum in the energy distribution curves (EDCs) to define the top of the β band which is located mainly below E_F. We observe that the α hole band clearly crosses the Fermi level (see Fig. 1d), whereas the spectral weight of the β band only emerges from $x \sim 0.15$ as a central peak in the MDC spectrum at E_F. In tetragonal FeSe the β band forms a 3D hole pocket, however upon entering the nematic phase this pocket is pushed below the Fermi-level[3,37]. By suppressing the nematic phase with S substitution, the β pocket re-emerges at $FeSe_{0.89}S_{0.11}$[3,37] However, with Te substitution, in which the nematic phase extends over a larger compositional range towards $x \sim 0.45$[34], the shift of this band is less pronounced. Interestingly, the γ band shifts significantly from a binding energy around 50 meV to 20 meV towards the Fermi level at both high symmetry points (see Fig. 1b and Supplementary Fig. 6) This is in contrast to findings for the $FeSe_{1-x}S_x$ series, where the γ band is relatively unaffected by isoelectronic substitution up to $x \sim 0.18$[38]. However, these findings are in good agreement with the prediction of the density functional theory (DFT) calculations which shows that the γ band only begins to shift for value of $h > 1.45$ Å (see Supplementary Fig. 3).

Figure 1e, f shows that the extracted band dispersions for the α and β hole bands become narrower, suggesting a decrease in the effective masses with increasing Te concentration. The extracted values of the Fermi wavevector, k_F, suggest that the size of the α hole pocket hardly varies with increasing Te concentration, consistent with studies at higher x values[39] (see Fig. 1d and Supplementary Fig. 6).

The nematic order parameter, φ_{nem} is usually estimated from the energy splitting between the α and β hole bands, given by $\Delta_h = \sqrt{\varphi_{nem}^2 + \lambda_1^2}$[40,41]. As the spin-orbit coupling (SOC) parameter, $\lambda_1 \sim 23.5$ meV for FeSe at high temperatures inside the tetragonal phase[13,20,42], and at low temperatures Δ_h increase towards 37.5 meV, the value of φ_{nem} was estimated as ~ 29 meV for FeSe[20,42]. With S isoelectronic substitution φ_{nem} decreases and at low temperatures the β hole band crosses the Fermi level and forms the 3D pocket at Z point[3,37,38]. In contrast, the Δ_h splitting for $FeSe_{1-x}Te_x$ remains around 38(3) meV due to two competing effects: one caused by the reduction in the nematic order

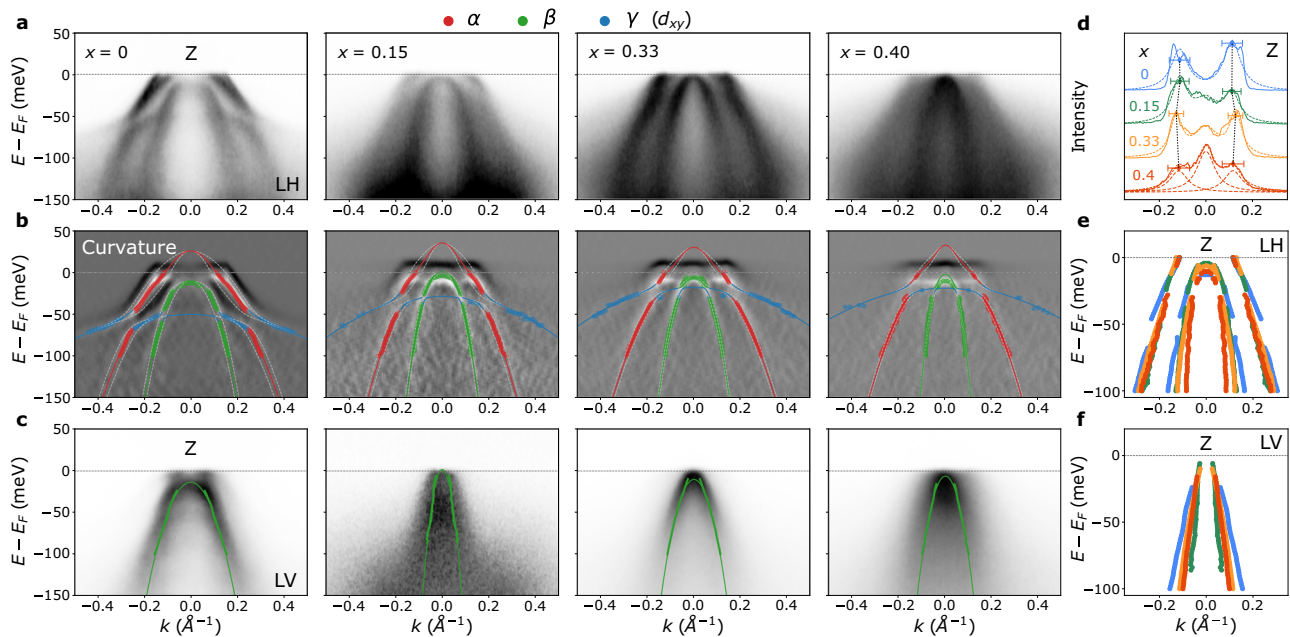**Fig. 1 Hole bands of nematic FeSe$_{1-x}$Te$_x$. a** Angle-resolved photoemission spectroscopy (ARPES) spectra measured at the Z high-symmetry point along the $A - Z - A$ direction at 10 K using linear horizontal (LH) light polarisation. **b** The corresponding two-dimensional curvature of the ARPES data from **a** using the method in ref. [35]. The solid points are the band positions extracted from Lorentzian fits to the momentum distribution curves (MDCs) (α and β bands), maximums in the energy distribution curves (EDCs) (β band) and extrema in the curvature of the EDCs (γ band). The solid lines are fits to the band positions using the low-energy model discussed in the Supplementary Note 2. **c** ARPES spectra for the same dispersions as in **a** but measured using linear vertical (LV) light polarisation. The solid points are the band positions extracted from MDC analysis, and the solid curve is a parabolic fit to the data. The solid lines in **b** and **c** corresponds to the outer hole band, α (red), the inner hole band, β (green) and the flatter d_{xy} hole band, γ (blue). **d** MDCs taken at the Fermi level to determine the Fermi wavevector (k_F) from **a**, where the errors are equal to half of the full-width half-maximum from the Lorentzian fits (dashed curves). **e** The extracted hole dispersions of the α and β bands for different x using LH polarisation. **f** The extracted β bands using LV polarisation. Different colours in **d**, **e** and **f** refer to the x compositions, as indicated in **d**.

parameter with increasing x and the second caused by the enhanced SOC splitting (DFT calculations predict a variation from 82 meV for FeSe to 177 meV for FeTe at the Z point, as shown in Supplementary Fig. 1).

The role of the chalcogen p_z band. The position of the p_z band and its interaction with the hole bands is complex and heavily dependent on the chalcogen height, h, which strongly changes with the Te concentration, x, as shown in Supplementary Figs. 1 and 2. The chalcogen p_z band, which is predicted to be located above the Fermi level at the Γ point in FeSe, intercepts vertically all three hole bands along the Γ − Z direction (see E_{p_z} in Supplementary Fig. 1). Due to symmetry reasons, the crossing between the inner hole band and the chalcogen p_z band is proposed to create a band inversion, allowing topological surface states to form[6,15]. Based on the DFT predictions, this crossing first occurs at the Z point for $h \approx 1.4$ Å, and its hybridisation with the inner hole band creates a gap (along the Z − A direction). As a consequence the p_z band and the inner hole band smoothly merge and their orbital characters mix, resulting in a pseudo-inner hole band having a larger degree of p_z orbital character[27].

In order to assess the contribution of the p_z band in experiments, we perform a quantitative analysis of the ARPES intensity of the β band in relation to the α band, $I(\beta, \alpha)$. This relative intensity is evaluated at the two high-symmetry points with different k_z values (Γ and Z) giving the ratio $I(\beta, \alpha)_Z / I(\beta, \alpha)_\Gamma$ (see Supplementary Note 3). We find this ratio to increase beyond $x = 0.33$, as shown in Fig. 1 and Supplementary Fig. 7. This variation in intensity indicates an alteration in the orbital character of the bands due to hybridisation with other bands. However, changes in intensity due to nematic effects and the

contribution from the γ band should manifest equally at the Γ and Z point. Thus, the variations in the intensity ratio suggest that the matrix elements have changed for the β band due to the interaction with the p_z band, which is strongly k_z dependent. This is in agreement with previous studies which have highlighted the presence of the p_z band at Z in $x \sim 0.55$[27,43,44]. Additionally, we observe the emergence of a central peak in the MDCs at E_F for $x \sim 0.15$, which could also be due to the enhanced intensity of the β band at Z.

The low-energy model and effective masses. In order to quantify the evolution of the electronic correlations and band shifts of the hole bands of FeSe$_{1-x}$Te$_x$ as a function of Te concentration, we employed a low energy three-band model to describe the effective masses of the α, β and γ bands. This model contains essentially three parabolic dispersions in the presence of SOC and the nematic order. This approach is an extension of the model developed from refs. [40,45,46] to accommodate the third hole band, γ, as detailed in Supplementary Note 2. To constrain the parameters of the model we fixed φ_{nem} to be proportional to the nematic transition temperature, T_s, such that $\varphi_{nem} = 29$ meV for FeSe, as reported in refs. [13,42]. This additional constraint was introduced to account for the fact that the nematic order parameter is difficult to estimate from the splitting between the α and β hole bands, Δ_h. This is caused by the lack of experimental data above the Fermi level and linewidth broadening caused by the impurity scattering and averaging over two different domains.

Figure 2 shows the extracted effective masses, m^*, from the three-band model as a function of Te concentration. For the α and β hole bands, m^* decreases with increasing Te substitution. This is similar to the renormalisation factor for the d_{z^2} band, as

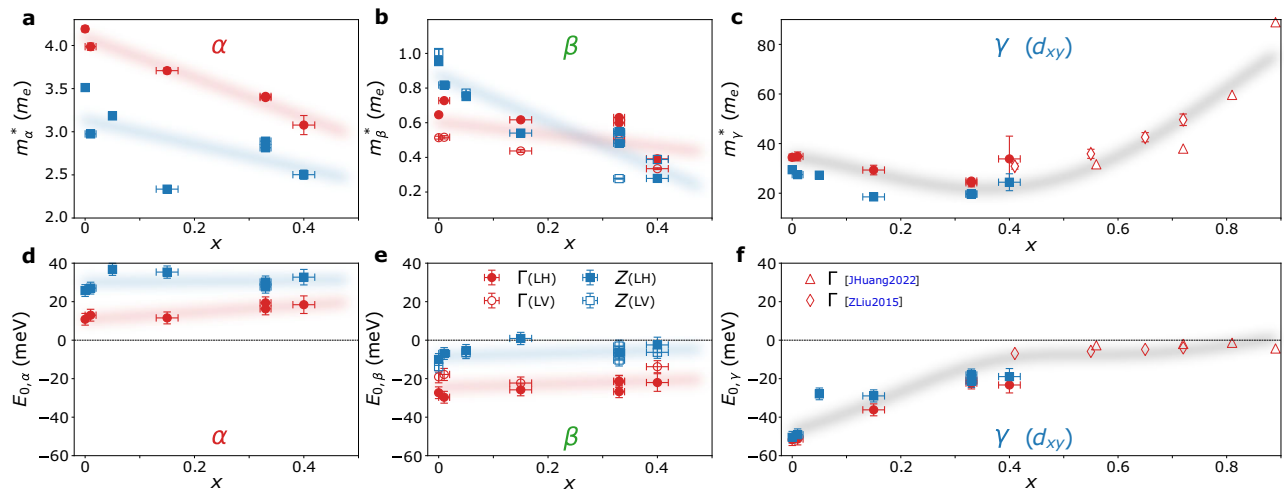**Fig. 2 Effective masses and Fermi energies of the hole bands.** The effective masses of the α band in **a**, the β band in **b** and the γ hole band in **c** as a function of Te concentration. The solid lines in **a** and **b** are linear fits for each data set at different high symmetry points, Γ (red circles) and Z (blue squares). Data for β are from both polarisations, with open and solid symbols corresponding to linear vertical and linear horizontal, respectively. The solid line in **c** is a 5th order polynomial fit to the data. Open diamond and triangles are from refs. [31] and [30], respectively. The Fermi energies of each band are plotted as a function of x in **d** ($E_{0,\alpha}$), **e** ($E_{0,\beta}$) and **f** ($E_{0,\gamma}$), where data from refs. [31] and [30] are added. The solid lines in **d** and **e** are linear fits, while the solid line in **f** is described by a phenomenological model detailed in the Discussion. The error bars in all plots are calculated from the covariance values produced within the non-linear least squares fitting function.

detailed in Supplementary Note 4. In contrast, the effective mass of the γ hole band displays a non-monotonic behaviour, as it decreases inside the nematic phase (from $x = 0$ towards a minimum close to $x \sim 0.3$) and then increases to values twice as large as those seen in FeSe at $x \sim 0.8$[30,31].

The renormalisation factors for each band can be estimated from the ratio of the experimental effective masses to the band masses evaluated from DFT calculations. The estimated values for FeSe are 3.5 and 1.8 for the α and β band, respectively, which is in close agreement to those previously reported[47]. However, for the γ band we determine a value $\sim$21, whereas previous studies give values between 8 and 10[13,47]. This discrepancy lies within our use of the curvature analysis, which gives us a larger momentum range to constrain the fit and our consideration for the SOC between the γ and α bands.

Evolution of the electron pockets. Figure 4a shows the evolution of the ARPES spectra corresponding to the electron pockets centred at the A high-symmetry point for different Te substitutions. We observe significant changes between the spectra for the different compositions, as compared with FeSe, in particular at high Te concentration ($x \sim 0.33$) where only one large electron pocket is detected. The DFT calculations in the tetragonal phase indicate that there are two degenerate points (A_1 corresponds to two bands with $d_{xz/yz}$ character whereas A_3 is for two bands of d_{xy} character)[40] (see Supplementary Fig. 1). The energy separation between spectral features along the EDC at the A point, defined as Δ_A, is therefore finite inside the tetragonal phase and found to be $\sim$20 meV for FeSe$_{0.82}$S$_{0.18}$[3]. However, as the nematic phase emerges the degeneracy of the two points are lifted (see Supplementary Fig. 10) the value of Δ_A has been originally interpreted as a parameter to quantify the nematic order[48–50], increasing towards $\sim$50 meV[13] in bulk FeSe or $\sim$70 meV in thin films of FeSe[49].

Figure 3e illustrates the estimation of Δ_A for different FeSe$_{1-x}$Te$_x$, from the EDC curves, as the separation between the two upper-most Lorentzian centres where the energy broadening is assumed to be linearly dependent on energy (see Supplementary Note 5). This linear energy dependence, often

associated to a marginal Fermi-liquid behaviour in iron-based superconductors[51], is evaluated by analysing the β hole band dispersion, as shown in Fig. 1c and Supplementary Fig. 6. Figure 3f shows that there is a direct correlation between Δ_A and the structural transition T_s, similar to FeSe$_{1-x}$S$_x$[3], which decreases as the nematic order is suppressed with increasing Te substitution. However, to assess the precise nematic electronic order parameter any additional splitting would need to be quantified for single domain detwinned samples under applied strain, as in the case of FeSe[9,40,46,48–50,52].

Figure 3d shows a comparison between the different band dispersions centred at the A point, using the extremal values from the curvature plots due to their weak features. Interestingly, we find the position of the hole-like band dispersion, ζ, remains unchanged up to $x \sim 0.33$, as shown in Fig. 3c, where this continues even for higher Te concentrations ($0.56 < x < 0.75$)[30]. Furthermore, only one electron pocket is resolved for higher x (using the MDC curves in Fig. 3b) and the k_F values increase with Te concentration. This is possibly due to the electron pockets becoming more isotropic as the nematic phase is suppressed. Additionally, the Fermi surface map of $x = 0.33$ (see Fig. 4d) shows that the size of the electron pockets relative to the hole pockets is larger, suggesting that the system may be slightly electron doped (the average k_F values for $x = 0.4$ is 0.12 Å^{-1} for the electron pockets and 0.09 Å^{-1} for the hole pockets).

Discussion
The phase diagram of FeSe$_{1-x}$Te$_x$ illustrates the suppression of the nematic phase with increasing the Te concentration, x, as shown in Fig. 4a. The superconducting transition temperature, T_c, decreases inside the nematic phase towards a minimum of $\sim$6 K around $x \sim 0.3$, followed by an increase towards 13 K above $x \sim 0.5$. This resurgent superconducting dome extends over a large range and becomes filamentary as the system approaches the bi-collinear magnetic order close to FeTe[53]. Figure 4c shows that the effective masses, m^* of the α, β and γ hole bands decrease by increasing x, which correlates with the reduction of the renormalisation factor associated the d_{z^2} hole band (shown in Supplementary Fig. 8). Interestingly, the reduction of the effective
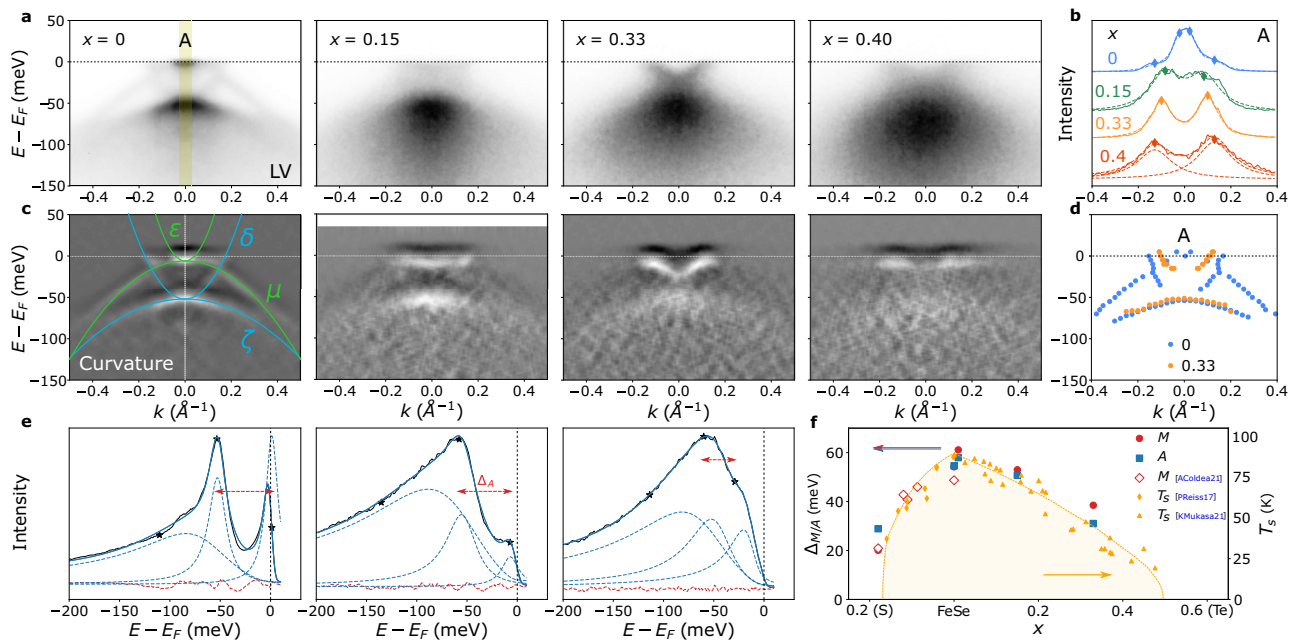
Fig. 3 Electron Pocket of FeSe$_{1-x}$Te$_x$. a Angle-resolved photoemission spectroscopy (ARPES) spectra taken at 10 K along the $Z - A - Z$ direction using linear vertical light polarisation for the different compositions, x. **b** Momentum distribution curves at the Fermi level for each x are plotted with solid curves and the dashed plots correspond to Lorentzian fits. The diamond data points indicate the Lorentzian centres, and thus the Fermi-wavevectors, k_F. **c** The two-dimensional curvature of the ARPES spectra in **a**. The different parabolic dispersions are labelled for the FeSe spectra. **d** The estimated band dispersion for $x = 0$ and $x = 0.33$, where the data is extracted from minima within curvature of the spectra. **e** The estimation of Δ_A by fitting the energy distribution curve (solid black curve) (integrated within the window indicated by the yellow strip for $x = 0$ in **a**). The blue solid curve is the fit, the dashed blue curves are the individual Lorentzian curves and dashed red plot is the residuals. Star data points correspond to the position of the Lorentzian centre. **f** The variation of Δ_A as a function of composition, x, (solid square) together with those for Δ_M (solid circles) from Supplementary Fig. 11. Additional data for FeSe$_{1-x}$S$_x$ (open red rhombuses) are taken from ref. [3]. The variation of T_s as a function of composition is plotted on right y-axis using data from refs. [38] (orange diamond) and[5] (orange triangle).

mass of the α hole band, which crosses the Fermi level, is accompanied by the suppression of superconductivity inside the nematic phase, suggesting this hole pocket is likely to be involved in the superconducting pairing. This is consistent with previous trends detected from quantum oscillations in FeSe$_{1-x}$S$_x$, where both the effective mass and the superconducting transition temperature, T_c, reach a maximum near $x \sim 0.1$, followed by a strong suppression towards FeS[3,38,54], as well as for FeSe$_{0.89}$S$_{0.11}$ under pressure[4].

The changes in the effective masses also reflect the potential role played by the chalcogen p_z band. The rate of decrease of the effective mass, m^*, for the α band with the Te concentration, x, is very similar for both high symmetry points. On the other hand, the effective mass for the lighter β band decreases faster at the Z point, as compared with the Γ point (Fig. 2b). When the p_z band intersects the β band the orbital mixing between the two is strongest at the Z point. As the p_z orbital is assumed to be less correlated than the Fe d orbitals[43], it is expected that the effective mass of the β band should be further reduced at the Z point relative to the Γ point, in agreement with the observed experimental trends.

Figures 4b and 2d–f show the Fermi energies, E_0, of the different bands estimated from the low-energy model as a function of x, indicating that α and β bands experience minimal variation. On the other hand, the γ band with the d_{xy} orbital character varies significantly and shifts towards the Fermi level up to $x \sim 0.4$, then it plateaus in its vicinity. Experimentally, there is a degree of uncertainty whether the γ band crosses the Fermi level[1,7,39] or not[30,31], and this discrepancy could be due to the amount of excess Fe in these systems[7]. Regardless, this is the region in the

phase diagram where the second superconducting dome is stabilised, suggesting that the hole band with d_{xy} orbital character could be involved in pairing. Furthermore, the strong shift of the γ band towards the Fermi level and the accompanying enhancement of superconductivity was also seen in thin films of FeSe$_{1-x}$Te$_x$/CaF$_2$[55].

To understand the significant shift towards the Fermi level of the γ band one can consider two mechanisms. Firstly, DFT predicts that the γ band moves up linearly with Te concentration, x, as the chalcogen height, h, increases and the lattice expands (see Supplementary Fig. 3). Secondly, variations of the bandwidth, due to electronic correlations, will also cause the Fermi energy to change, which can be crudely scaled as $\sim 1/m^*$. Thus, by combining the effect of the lattice and of the electronic correlations, the changes in the position of the γ band could be described by a phenomenological model, $E_\gamma(x) = \nu_1 x + \nu_2/m_\gamma^*(x) + \nu_3$. Figure 4c shows a fit to the experimental positions of the γ band, where ν_1 is the weight of the lattice effect, ν_2 is the weight of the bandwidth and ν_3 is an arbitrary offset ($m_\gamma^*(x)$ is taken as the 5th order polynomial fit from Fig. 2c). We find the fit captures the initial increase followed by a plateau for $x > 0.4$. For even higher x values a new hole-like pocket with d_{z^2} orbital character was detected at the X point for $x \geq 0.8$ due to the increase in electronic correlations which leads to the loss of the spectral weight of the d_{xy} band[31].

The presence of the third hole band with d_{xy} orbital close to the Fermi level and its involvement in pairing could manifest in different ways. Firstly, the hybridisation of the α hole band with the γ band would lead to a reduction in the Fermi velocity, thus increasing the density of states and enhancing superconductivity.
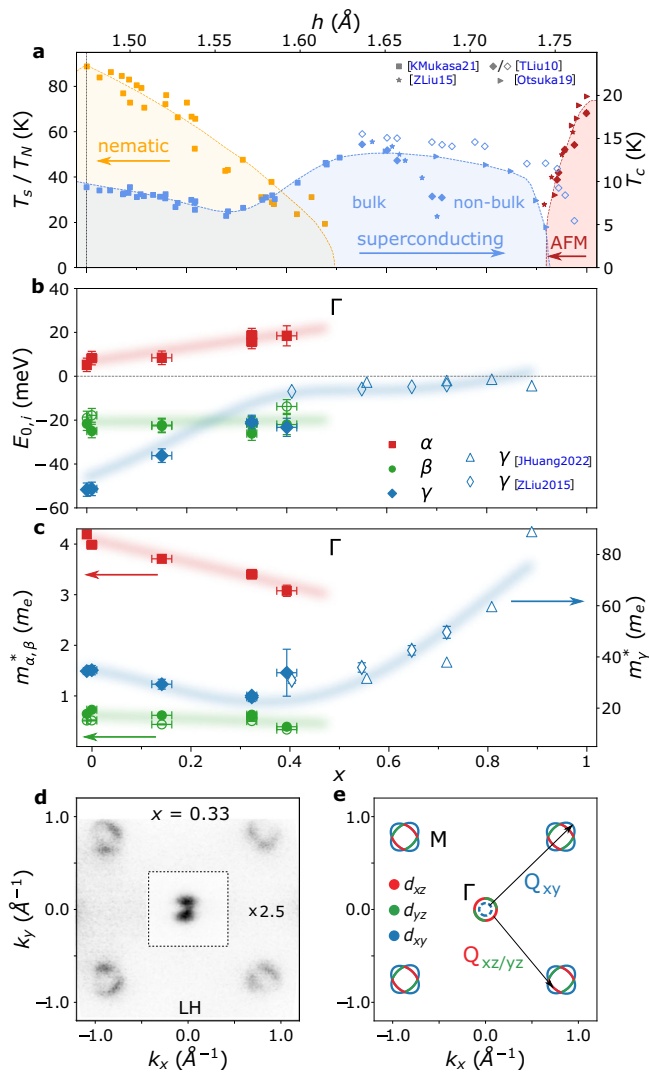
Fig. 4 Evolution of electronic structure and correlations in FeSe$_{1-x}$Te$_x$. **a** Phase diagram of FeSe$_{1-x}$Te$_x$, indicating the nematic phase transition (T_s, orange squares), the superconducting transition (T_c, blue points) and the antiferromagnetic phase transition (T_N, red points). Data points are taken from refs. [5,53,30,60]. **b** Fermi energies as a function of composition, x, for the α band (solid red squares), β band (solid and open green circles extracted from the linear horizontal (LH) and linear vertical (LV) spectra) and γ band (solid blue rhombuses). Additional points for γ band are from refs. [31] (blue triangles) and [30] (diamonds). The solid red and green lines are linear fits, while the blue curve is a 5th order polynomial fit. **c** Effective masses as a function of composition, x, where the symbols are defined as in **b**. The solid red and green lines are linear fits, while the blue curve is the phenomenological fit detailed in the discussion. In **b** and **c** only Γ data are shown, where the error bars are calculated from the covariance values produced within the non-linear least squares fitting function. **d** Fermi surface map of the first Brillouin zone for $x = 0.33$ taken at 10 K using angle-resolved photoemission spectroscopy with LH polarisation. The spectra outside of the dashed box is enhanced by a factor of 2.5. **e** Schematic Fermi surface indicating the dominant orbital character of each potion of the bands and potential pairing channels.

Secondly, the orbital mixing between these bands would open up a new pairing channel which connects to the d_{xy} orbital character at the electron pocket with the hole pockets (see Fig. 4e). Thirdly, a new pairing channel could be achieved if $E_{0,\gamma}$ is smaller than the superconducting gap, as in this regime the γ band can play the

role of an incipient band[56]. The superconducting pairing in FeSe is proposed to be mediated by spin fluctuations between the hole and electron pockets with d_{yz} orbital character along $\overrightarrow{Q}_{xy/yz} = (\pi, \pi)$ (Fig. 4d and e)[17,23,24,57]. A similar vector, $\overrightarrow{Q}_{xy}$, that would connect the d_{xy} channel, and the observation of stripe magnetic fluctuations in FeSe$_{1-x}$Te$_x$ could suggest that the second superconducting dome may also be driven by spin fluctuations[53,58,59]. However, neutron scattering studies also observe the development of $(\pi, 0)$ spin fluctuations which compete with superconductivity[53]. This competition is evident as the suppression of superconductivity, towards FeTe, is accompanied by the development of a double-stripe magnetic order with a $(\pi, 0)$ wave vector[60].

There is a strong contrast between the FeSe$_{1-x}$Te$_x$ and FeSe$_{1-x}$S$_x$ series, which displays no enhancement of T_c outside the nematic phase and the d_{xy} hole band is located 50 meV below the Fermi level[3]. On the other hand, quantum oscillations found a direct correlation between the evolution of the effective mass of the α band and T_c in FeSe$_{1-x}$S$_x$[54], which also occurs inside the nematic phase of FeSe$_{1-x}$Te$_x$. These trends change significantly in the vicinity of the nematic end point of FeSe$_{1-x}$Te$_x$ ($x \sim 0.5$), as the effective masses for the α and β hole bands remain rather constant[30,31], whereas the superconductivity is enhanced (see Fig. 4a). On the other hand, both the effective mass for the γ band and T_c increase at a similar composition x. This suggests that the mechanism for superconductivity likely changes across the phase diagram of FeSe$_{1-x}$Te$_x$[30,61] and the hole band γ, with d_{xy} orbital character, plays an important role.

An alternative mechanism for the enhancement of superconductivity can be related to its proximity to the nematic end point. Theoretically, nematic fluctuations should support superconductivity in both an s or d-wave pairing channel[1,19], and elastoresistivity studies find a divergence of the nematic susceptibility near its end point[34]. However, studies of FeSe$_{0.89}$S$_{0.11}$ under pressure suggest the critical fluctuations could either be quenched via the coupling of the nematic order to the lattice[4] or obscured within the nematic islands of a quantum Griffiths phase[62]. Moreover, other hallmarks of a quantum critical point in FeSe$_{1-x}$Te$_x$, such as the divergence of the effective masses at the nematic end point and/or a linear dependence of resistivity in temperature are not observed[5]. These systems are rather bad metals, with large linewidths in the ARPES spectra, which could be caused by the large distribution of the Se and Te ions (chalcogen heights differ by 0.24 Å)[63] and the stabilisation of the interstitial Fe that could act as additional scattering centres.

The evolution of the band structure and the significant shifts of the d_{xy} band via Te substitution have implications on other studies. The chalcogen height h is an important parameter that influences the changes in the band structure, magnetic ground state and superconductivity[26,64]. For example, h, could be shifted towards higher values with applied pressure in other iron chalcogenides, despite the shrinking of the unit cell. Theoretical studies of FeSe and NMR studies of FeSe$_{0.88}$S$_{0.12}$ have suggested that the hole d_{xy} band could lead to the enhanced superconducting dome induced by pressure[65,66]. However, pressure also induces magnetic order and the maximum in T_c is often located at the end point of the magnetic phase in FeSe$_{1-x}$S$_x$[5,67], suggesting that magnetic fluctuations are important for superconducting pairing.

Conclusion

In this study we present a comprehensive investigation of the low-temperature band structure of the nematic FeSe$_{1-x}$Te$_x$ series.

We identify a direct correlation between the changes in the nematic transition with the spectral features in the dispersions at the corner of the Brillouin zone, in agreement with other studies on iron-chalcogenide superconductors. Additionally, the changes in the relative intensities of spectra corresponding to the inner and outer hole bands reflect the contribution of the p_z band, as it is brought towards the Fermi level by increasing Te concentration.

By using a low-energy three-band model, which captures much of the underlying electronic properties, we extract the effective mass for the hole bands that show an unexpected decrease inside the nematic phase. These findings are consistent with the decrease in the renormalisation associated the higher energy d_{z^2} bands. On the other hand, the effective mass of the third hole band with d_{xy} orbital character has a local minimum before increasing significantly in the tetragonal region. Concomitantly, we detect the gradual shift of this, rather flat, d_{xy} hole band towards the Fermi-level with increasing Te concentration, which could lead to an enhancement of the density of states and the opening of a new pairing channel. This effect could be responsible for the emergence of the second superconducting dome outside the nematic phase involving the hole band with d_{xy} orbital character, in contrast to the superconducting dome inside the nematic phase. These trends occur at the same time as the chalcogen height increases, and our findings may have implications for other studies, like those under applied pressure. Moreover, at high Te concentration, the resistivity of $FeSe_{1-x}Te_x$ reflects bad metallic behaviour but superconductivity remains rather robust. Our findings suggest changes in the superconducting mechanism between that emerging from the nematic phase, with rather weak electronic correlations, and the second superconducting dome outside the nematic phase. Further theoretical studies that aim to understand the superconducting mechanisms in these systems could consider the presence of the orbitally dependent electronic correlations, the enhanced density of states induced by a nearly-flat band with d_{xy} orbital character and potentially the significant effects caused by the local variation in the chalcogen height.

Methods

Sample characterisation. Single crystals of $FeSe_{1-x}Te_x$ were grown via the new chemical vapour transport method[68] and screened via transport studies and X-ray diffraction (XRD). The nematic transition, T_s was evaluated from the temperature dependence of the longitudinal resistivity (as the extremum in the first derivative as a function of temperature) as well as from X-ray studies, and compared with a previous report[5]. After each ARPES experiment, we also performed Energy Dispersive X-ray (EDX) spectroscopy studies to directly measure the composition of each investigated crystal and these values are reported here.

ARPES measurements were performed at the I05 beamline at the Diamond Light Source synchrotron using a MBS A1 hemispherical analyser giving a combined energy resolution of ~3 meV[69]. The incident photon energy was varied between 23–100 eV to probe the k_z dependence of the electronic structure and to identify the high-symmetry points. The single crystals were cleaved in-situ using a top-post and all measurements were performed at the base temperature of 10 K and under ultrahigh vacuum at 10^{-10} mbar. The beamspot was ~50 μm which is much larger than the nematic domains of the samples[70]. Therefore, all spectra are a superposition of the two orthogonal domains. Besides the reported data on new crystals of $FeSe_{1-x}Te_x$, we compare our results to previous ARPES data on FeSe from refs. [13,20] and the tetragonal system, $FeSe_{0.82}S_{0.18}$, reported previously in refs. [3,38].

Density functional theory. To complement the experimental data, we have performed DFT band structure calculations using the Wien2k software in the GGA approximation with and without SOC[71] which are presented in Supplementary Note 1. These calculations were performed in the tetragonal phase with lattice parameters taken from refs. [5,38,72], as listed in Supplementary Table 1.

References

1. Tamai, A. et al. Strong electron correlations in the normal state of the iron-based $FeSe_{0.42}Te_{0.58}$ superconductor observed by angle-resolved photoemission spectroscopy. *Phys. Rev. Lett.* **104**, 097002 (2010).
2. Yi, M. et al. Observation of universal strong orbital-dependent correlation effects in iron chalcogenides. *Nat. Commun.* **6**, https://doi.org/10.1038/ncomms8777 (2015).
3. Coldea, A. I. Electronic Nematic States Tuned by Isoelectronic Substitution in Bulk $FeSe_{1-x}S_x$. *Frontiers in Physics.* **8** https://doi.org/10.3389/fphy.2020.594500 (2021).
4. Reiss, P. et al. Quenched nematic criticality and two superconducting domes in an iron-based superconductor. *Nat. Phys.* **16**, 89–94 (2020).
5. Mukasa, K. et al. High-pressure phase diagrams of $FeSe_{1-x}Te_x$: correlation between suppressed nematicity and enhanced superconductivity. *Nat. Commun.* 1–7, https://doi.org/10.1038/s41467-020-20621-2 (2021).
6. Zhang, P. et al. Observation of topological superconductivity on the surface of an iron-based superconductor. *Science* **360**, 182–186 (2018).
7. Rinott, S. et al. Tuning across the BCS-BEC crossover in the multiband superconductor $Fe_{1+y}Se_xTe_{1-x}$: an angle-resolved photoemission study. *Sci. Adv.* **3**, e1602372 (2017).
8. Fernandes, R. M. & Vafek, O. What drives nematic order in iron-based superconductors? *Nat. Phys.* **10**, 97–104 (2014).
9. Fedorov, A. et al. Effect of nematic ordering on electronic structure of FeSe. *Sci. Rep.* **6**, 36834 (2016).
10. Kuo, H.-H., Chu, J.-H., Palmstrom, J. C., Kivelson, S. A. & Fisher, I. R. Ubiquitous signatures of nematic quantum criticality in optimally doped Fe-based superconductors. *Science* **352**, 958–962 (2016).
11. Bartlett, J. M. et al. Relationship between transport anisotropy and nematicity in FeSe. *Phys. Rev. X* **11**, 021038 (2021).
12. Ghini, M. et al. Strain tuning of nematicity and superconductivity in single crystals of FeSe. *Phys. Rev. B* **103**, 205139 (2021).
13. Watson, M. D. et al. Emergence of the nematic electronic state in FeSe. *Phys. Rev. B* **91**, 155106 (2015).
14. Böhmer, A. E., Chu, J.-H., Lederer, S. & Yi, M. Nematicity and nematic fluctuations in iron-based superconductors. *Nat. Phys.* **18**, 1412–1419 (2022).
15. Fernandes, R. M. et al. Iron pnictides and chalcogenides: a new paradigm for superconductivity. *Nature* **601**, 35–44 (2022).
16. Shibauchi, T., Carrington, A. & Matsuda, Y. A quantum critical point lying beneath the superconducting dome in iron pnictides. *Annu. Rev. Condens. Matter Phys.* **5**, 113–135 (2014).
17. Gu, Y. et al. Unified phase diagram for iron-based superconductors. *Phys. Rev. Lett.* **119**, 157001 (2017).
18. Malinowski, P. et al. Suppression of superconductivity by anisotropic strain near a nematic quantum critical point. *Nat. Phys.* **16**, 1189–1193 (2020).
19. Labat, D. & Paul, I. Pairing instability near a lattice-influenced nematic quantum critical point. *Phys. Rev. B* **96**, 195146 (2017).
20. Coldea, A. I. & Watson, M. D. The key ingredients of the electronic structure of FeSe. *Annu. Rev. Condens. Matter Phys.* **9**, 125–146 (2018).
21. Sprau, P. O. et al. Discovery of orbital-selective Cooper pairing in FeSe. *Science* **357**, 75–80 (2017).
22. Kreisel, A., Hirschfeld, P. J. & Andersen, B. M. On the remarkable superconductivity of FeSe and its close cousins. *Symmetry* **12**, 1402 (2020).
23. Rhodes, L. C. et al. Scaling of the superconducting gap with orbital character in FeSe. *Phys. Rev. B* **98**, 180503 (2018).

24. Wang, Q. et al. Strong interplay between stripe spin fluctuations, nematicity and superconductivity in FeSe. *Nat. Mater.* **15**, 159–163 (2016).

25. Zajicek, Z. et al. Drastic effect of impurity scattering on the electronic and superconducting properties of Cu-doped FeSe. *Phys. Rev. B* **105**, 115130 (2022).

26. Kumar, J., Auluck, S., Ahluwalia, P. K. & Awana, V. P. S. Chalcogen height dependence of magnetism and Fermiology in FeTe$_x$Se$_{1-x}$. *Supercond. Sci. Technol.* **25**, 095002 (2012).

27. Wang, Z. et al. Topological nature of the FeSe$_{0.5}$Te$_{0.5}$ superconductor. *Phys. Rev. B* **92**, 115119 (2015).

28. Lauke, L. et al. Band engineering of Dirac cones in iron chalcogenides. *Phys. Rev. B* **102**, 054209 (2020).

29. Chen, C. et al. Atomic line defects and zero-energy end states in monolayer Fe(Te,Se) high-temperature superconductors. *Nat. Phys.* **16**, 536–540 (2020).

30. Liu, Z. K. et al. Experimental observation of incoherent-coherent crossover and orbital-dependent band renormalization in iron chalcogenide superconductors. *Phys. Rev. B* **92**, 235138 (2015).

31. Huang, J. et al. Correlation-driven electronic reconstruction in FeTe$_{1-x}$Se$_x$. *Commun. Phys.* **5**, https://doi.org/10.1038/s42005-022-00805-6 (2022).

32. Xing, X. et al. Electronic transport properties and hydrostatic pressure effect of FeSe$_{0.67}$Te$_{0.33}$ single crystals free of phase separation. *Supercond. Sci. Technol.* **34**, 055006 (2021).

33. Ovchenkov, Y. A. et al. Phase separation near the charge neutrality point in FeSe$_{1-x}$Te$_x$ crystals with $x < 0.15$. *Supercond. Sci. Technol.* **35**, 015011 (2021).

34. Ishida, K. et al. Pure nematic quantum critical point accompanied by a superconducting dome. *Proc. Natl Acad. Sci.* **119**, e2110501119 (2022).

35. Zhang, P. et al. A precise method for visualizing dispersive features in image plots. *Rev. Sci. Instrum.* **82**, 043712 (2011).

36. Zhang, Y. et al. Symmetry breaking via orbital-dependent reconstruction of electronic structure in detwinned NaFeAs. *Phys. Rev. B* **85**, 085121 (2012).

37. Watson, M. D. et al. Suppression of orbital ordering by chemical pressure in FeSe$_{1-x}$S$_x$. *Phys. Rev. B* **92**, 121108 (2015).

38. Reiss, P. et al. Suppression of electronic correlations by chemical pressure from FeSe to FeS. *Phys. Rev. B* **96**, 121103 (2017).

39. Ieki, E. et al. Evolution from incoherent to coherent electronic states and its implications for superconductivity in FeTe$_{1-x}$Se$_x$. *Phys. Rev. B* **89**, 140506 (2014).

40. Fernandes, R. M. & Vafek, O. Distinguishing spin-orbit coupling and nematic order in the electronic spectrum of iron-based superconductors. *Phys. Rev. B* **90**, 214514 (2014).

41. Xing, R.-Q., Classen, L., Khodas, M. & Chubukov, A. V. Competing instabilities, orbital ordering, and splitting of band degeneracies from a parquet renormalization group analysis of a four-pocket model for iron-based superconductors: application to FeSe. *Phys. Rev. B* **95**, 085108 (2017).

42. Watson, M. D. et al. Shifts and splittings of the hole bands in the nematic phase of FeSe. *J. Phys. Soc. Jpn.* **86**, 053703 (2017).

43. Lohani, H. et al. Band inversion and topology of the bulk electronic structure in FeSe$_{0.45}$Te$_{0.55}$. *Phys. Rev. B* **101**, 245146 (2020).

44. Li, Y. F. et al. Spectroscopic evidence for topological band structure in FeTe$_{0.55}$Se$_{0.45}$. *arXiv*, https://arxiv.org/abs/2307.03861 (2023).

45. Cvetkovic, V. & Vafek, O. Space group symmetry, spin-orbit coupling, and the low-energy effective Hamiltonian for iron-based superconductors. *Phys. Rev. B* **88**, 134510 (2013).

46. Rhodes, L. C., Böker, J., Müller, M. A., Eschrig, M. & Eremin, I. M. Non-local d$_{xy}$ nematicity and the missing electron pocket in FeSe. *npj Quantum Mater.* **6**, 45 (2021).

47. Maletz, J. et al. Unusual band renormalization in the simplest iron-based superconductor FeSe$_{1-x}$. *Phys. Rev. B* **89**, 220506 (2014).

48. Yi, M. et al. Nematic energy scale and the missing electron pocket in FeSe. *Phys. Rev. X* **9**, 041049 (2019).

49. Zhang, Y. et al. Distinctive orbital anisotropy observed in the nematic state of a FeSe thin film. *Phys. Rev. B* **94**, 115153 (2016).

50. Watson, M. D. et al. Evidence for unidirectional nematic bond ordering in FeSe. *Phys. Rev. B* **94**, 201107 (2016).

51. Fink, J. et al. Linkage between scattering rates and superconductivity in doped ferropnictides. *Phys. Rev. B* **103**, 155119 (2021).

52. Christensen, M. H., Fernandes, R. M. & Chubukov, A. V. Orbital transmutation and the electronic spectrum of FeSe in the nematic phase. *Phys. Rev. Res.* **2**, 013015 (2020).

53. Liu, T. J. et al. From $(\pi,0)$ magnetic order to superconductivity with (π,π) magnetic resonance in Fe$_{1.02}$Te$_{1-x}$Se$_x$. *Nat. Mater.* **9**, 718–720 (2010).

54. Coldea, A. et al. Evolution of the low-temperature Fermi surface of superconducting FeSe$_{1-x}$S$_x$ across a nematic phase transition. *npj Quantum Mater.* **4**, 2 (2019).

55. Nakayama, K. et al. Orbital mixing at the onset of high-temperature superconductivity in FeSe$_{1-x}$Te$_x$/CaF$_2$. *Phys. Rev. Res.* **3**, L012007 (2021).

56. Chen, X., Maiti, S., Linscheid, A. & Hirschfeld, P. J. Electron pairing in the presence of incipient bands in iron-based superconductors. *Phys. Rev. B* **92**, 224514 (2015).

57. Mazin, I. I., Singh, D. J., Johannes, M. D. & Du, M. H. Unconventional superconductivity with a sign reversal in the order parameter of LaFeAsO$_{1-x}$F$_x$. *Phys. Rev. Lett.* **101**, 057003 (2008).

58. Li, Y. et al. Electronic properties of the bulk and surface states of Fe$_{1+y}$Te$_{1-x}$Se$_x$. *Nat. Mater.* **20**, 1221–1227 (2021).

59. Argyriou, D. N. et al. Incommensurate itinerant antiferromagnetic excitations and spin resonance in the FeTe$_{0.6}$Se$_{0.4}$ superconductor. *Phys. Rev. B* **81**, 220503 (2010).

60. Otsuka, T. et al. Incoherent-coherent crossover and the pseudogap in Te-annealed superconducting Fe$_{1+y}$Te$_{1-x}$Se$_x$ revealed by magnetotransport measurements. *Phys. Rev. B* **99**, 184505 (2019).

61. Yin, Z. P., Haule, K. & Kotliar, G. Kinetic frustration and the nature of the magnetic and paramagnetic states in iron pnictides and iron chalcogenides. *Nat. Mater.* **10**, 932–935 (2011).

62. Reiss, P., Graf, D., Haghighirad, A. A., Vojta, T. & Coldea, A. I. Signatures of a Quantum Griffiths Phase Close to an Electronic Nematic Quantum Phase Transition. *Phys. Rev. Lett.* **127**, 246402 (2021).

63. Tegel, M., Löhnert, C. & Johrendt, D. The crystal structure of FeSe$_{0.44}$Te$_{0.56}$. *Solid State Commun.* **150**, 383–385 (2010).

64. Kuroki, K., Usui, H., Onari, S., Arita, R. & Aoki, H. Pnictogen height as a possible switch between high-T_c nodeless and low-T_c nodal pairings in the iron-based superconductors. *Phys. Rev. B* **79**, 224511 (2009).

65. Yamakawa, Y. & Kontani, H. Nematicity, magnetism, and superconductivity in FeSe under pressure: Unified explanation based on the self-consistent vertex correction theory. *Phys. Rev. B* **96**, 144509 (2017).

66. Kuwayama, T. et al. Pressure-induced reconstitution of Fermi surfaces and spin fluctuations in S-substituted FeSe. *Sci. Rep.* **11**, 17265 (2021).

67. Matsuura, K. et al. Maximizing Tc by tuning nematicity and magnetism in FeSe$_{1-x}$S$_x$ superconductors. *Nat. Commun.* **8**, 1143 (2017).

68. Terao, K., Kashiwagi, T., Shizu, T., Klemm, R. A. & Kadowaki, K. Superconducting and tetragonal-to-orthorhombic transitions in single crystals of FeSe$_{1-x}$Te$_x$($0 \le x$($0 \le$. *Phys. Rev. B* **100**, 224516 (2019).

69. Hoesch, M. et al. A facility for the analysis of the electronic structures of solids and their surfaces by synchrotron radiation photoelectron spectroscopy. *Rev. Sci. Instrum.* **88**, https://doi.org/10.1063/1.4973562 (2017).

70. Rhodes, L. C., Watson, M. D., Haghighirad, A. A., Evtushinsky, D. V. & Kim, T. K. Revealing the single electron pocket of FeSe in a single orthorhombic domain. *Phys. Rev. B* **101**, 235128 (2020).

71. Blaha, P. et al. WIEN2k: an APW+lo program for calculating the properties of solids. *J. Chem. Phys.* **152**, 074101 (2020).

72. Li, S. et al. First-order magnetic and structural phase transitions in Fe$_{1+y}$Se$_x$Te$_{1-x}$. *Phys. Rev. B* **79**, 054503 (2009).

73. Richards, A. University of Oxford Advanced Research Computing Service https://doi.org/10.5281/zenodo.22558 (2023).

74. Morfoot, A., Kim, T. & Coldea, A. Resurgence of superconductivity and the role of the d$_{xy}$ hole band in FeSe1-xTex, https://doi.org/10.5287/ora-e9k5bn9e8.

Author contributions

A.B.M., T.K., M.D.W., A.I.C. performed ARPES measurements. A.A.H., S.J.S. grew the crystals; A.B.M. analysed the ARPES data; A.B.M., T.K., M.D.W., A.I.C. discussed the results and manuscript preparation. A.B.M. and A.I.C. wrote the manuscript with contributions from all authors.

Competing interests

The authors declare no competing interests.

Additional information

Supplementary information The online version contains supplementary material available at https://doi.org/10.1038/s42005-023-01481-w.

Correspondence and requests for materials should be addressed to Archie B. Morfoot or Amalia I. Coldea.

Peer review information *Communications Physics* thanks the anonymous reviewers for their contribution to the peer review of this work.

Reprints and permission information is available at http://www.nature.com/reprints

Publisher's note Springer Nature remains neutral with regard to jurisdictional claims in published maps and institutional affiliations.